Acta Mechanica Sinica (2021) 37(11):1637–1647
https://doi.org/10.1007/s10409-021-01136-5

RESEARCH PAPER

Design and transition characteristics of a standard model for hypersonic boundary layer transition research

Shenshen Liu[1,2] · Xianxu Yuan[1] · Zhiyong Liu[3] · Qiang Yang[1] · Guohua Tu[1] · Xi Chen[1] · Yewei Gui[1] · Jianqiang Chen[1,2]

Received: 22 June 2021 / Accepted: 8 July 2021 / Published online: 20 October 2021

Abstract
To understand fundamental problems in hypersonic laminar-turbulent boundary layer transition for three-dimensional complex vehicles, a new standard model with typical lifting-body features has been proposed, named as hypersonic transition research vehicle (HyTRV). The configuration of HyTRV is fully analytical, and details of the design process are discussed in this study. The transition characteristics for HyTRV are investigated using three combined methods, i.e., theoretical analyses, numerical simulations, and wind tunnel experiments. Results show that the fully analytic parameterization design of HyTRV can satisfy the model simplification requirements from both numerical simulations and wind tunnel experiments. Meanwhile, the flow field of HyTRV reveals typical transition mechanisms in six relatively separated regions, including the streamwise vortex instability, crossflow instability, secondary instability, and attachment-line instability. Therefore, the proposed HyTRV model is valuable for fundamental researches in hypersonic boundary layer transition.

Keywords Hypersonic boundary layer · Transition research · Standard model design · HyTRV

1 Introduction

Hypersonic laminar-turbulent boundary layer transition has been an unsolved problem in fluid mechanics for a long time [1–3]. Due to the significant differences in flow characteristics (such as the skin friction, noise level, heat transfer rate, and mixing efficiency) between a laminar boundary layer and a turbulent one [4], the designed weight of the thermal protection system of a hypersonic flight vehicle can deviate dramatically based on different transition prediction methods, which can directly affect the safety and performance of hypersonic flight vehicles. Meanwhile, the laminar-turbulent transition also plays an important role in the hypersonic propulsion system, and has effects on the inlet flow rate, the starting of the air-intaken, and the combustion efficiency. Therefore, the hypersonic boundary layer transition study is crucial for improving our understanding in the transition mechanism, as well as the transition prediction capability for many applications [5,6].

Different approaches can be used for the hypersonic boundary layer transition research, including wind tunnel experiments, numerical analyses, and model flight tests. Wind tunnels for the transition study can be categorized into two groups based on the noise level, i.e., conventional wind tunnels and quiet wind tunnels. Conventional wind tunnels (such as high enthalpy wind tunnels) can be used for experiments of large-scale models under the condition of high enthalpy and high Reynolds numbers, but the noise level of the incoming flow is much higher than that under flight conditions. On the contrary, the noise level of quiet wind tunnels is closer to the flight condition, but transition experiments can only be conducted for medium-sized models at the condition of low enthalpy and low incoming flow Reynolds numbers. Thus far, there is no such a wind tunnel that can fully reproduce the flight condition, therefore, the extrapolation of the transition data from the wind tunnel condition to the flight condition still remains a difficult issue [7].

Executive Editor: Yue Yang.

✉ Jianqiang Chen
chenjq@cardc.cn

[1] State Key Laboratory of Aerodynamics, China Aerodynamics Research and Development Center, Mianyang 621000, China

[2] Computational Aerodynamics Institute, China Aerodynamics Research and Development Center, Mianyang 621000, China

[3] China Academy of Aerospace Aerodynamics, Beijing 100074, China

Numerical analyses cover three aspects, i.e., stability analyses, numerical simulations, and transition models. Popular stability analysis methods include the traditional linear stability theory (LST) [8], parabolic stability equations (PSE) [9], and global stability analysis (BiGlobal/TriGlobal) [10]. Besides the above linear theory based methods, there are also nonlinear analysis tools including nonlinear parabolic stability equations (NPSE), secondary instability analysis methods (such as Floquet analysis) [11], and high Reynolds number asymptotic analysis methods [12], which are mainly suitable for flows in the weakly nonlinear regime. Numerical simulations can capture the richest transition details with fewest assumptions but at the cost of a large amount of computation resource, thus such a method is mainly used for simple flow configurations [13]. As the freestream noise level during the flight is unknown, the receptivity process is ambiguous, thus numerical simulations cannot fully reproduce the boundary layer transition phenomenon under real conditions. Based on experimental and numerical transition data, a variety of transition prediction models have been developed, such as the LST based eN method [14], the RANS framework based Fu-Wang model [15], and the γ-Re_θ model [16,17]. These models can achieve a good prediction accuracy under specific working conditions, but none of them can make a universal and robust transition prediction for general flows, which is mainly due to the existence of unknown empirical parameters, as well as the missing physics behind the transition criterion used in each model [18]. Therefore, wind tunnel experiments and numerical analyses alone cannot fully reveal the transition mechanism for real flight vehicles, and it is necessary to use model flight tests to carry out transition studies under flight conditions, especially with real freestream disturbances.

The flight model, with typical characteristics of real flight vehicles, is the foundation of each flight test, as it directly determines whether the flight test can obtain relevant phenomena, mechanisms and cognition of the transition problem, and whether it can achieve the expected research goals. There has been a series of flight test programs carried out internationally for the study of hypersonic boundary layer transition, such as HIFiRE (US-Australia cooperated), EXPERT (European Space Agency), HyBoLT (US), BOLT (US) [19–22]. By going through these research models, HIFiRE-1 is a conical configuration, HyBoLT is a flat-plate configuration, HIFiRE-5 is an elliptical cone configuration, EXPERT is a reentry blunt body configuration, and BOLT is a concave configuration with a small curvature and a swept leading edge. With the complexity increase of these transition research flight models in configurations, the crossflow effect becomes more obvious to support the improvement in the transition prediction capability. The China Aerodynamics Research and Development Center (CARDC) successfully launched the first domestic transition flight test of a cone model (MF-1) in 2015 [23], and obtained the boundary layer transition data for Mach numbers larger than 5, laying a foundation for the transition study via flight tests. Besides that, a correlation between the wind tunnel experiment and the flight test of boundary layer transition has been proposed based on the eN method [23].

With the improvement of computation power, the numerical analysis approach has gradually expanded to complex three-dimensional boundary layers, such as the elliptical cone, the circular cone at large angles of attack, and the BoLT [24–27]. In three-dimensional boundary layers, there are many different transitional regimes, such as the streamwise vortex, the crossflow, and the attachment line, which largely remain unclear. Therefore, the present work focus on the design of such a hypersonic boundary layer transition model, with the aim to support the transition research of three-dimensional complex configurations, as well as some possible future flight tests. Under the constraints of both a simple configuration and some distinctive features, the layout design and the parametric modelling method are studied, and a model with the characteristics of typical lifting-body flight vehicles is proposed, which is named as hypersonic transition research vehicle, abbreviated for HyTRV. Chen et al. [28] have carried out a one-dimensional stability analysis for the HyTRV model. Here, we further show the typical transition flow characteristics of HyTRV through a combined investigation of the linear stability analysis, numerical simulation, and wind tunnel experiment. All the transition data confirm that HyTRV is a successful design for the hypersonic boundary layer transition research.

2 Fully analytical design of HyTRV model

2.1 Aerodynamic configuration design

Over half a century, different missions, propulsion systems, flight models, launching platforms, etc., have led to the innovative and diversified development of the aerodynamic layout of hypersonic vehicles. Overall, in order to pursue higher aerodynamic efficiency, the layout of hypersonic aircraft has been continuously developed from an axisymmetric shape to a flattened lifting body, and the waverider is the current design limit as it can get the highest lift-to-drag ratio [29]. In addition to the reentry capsules and warheads, the lifting body plays an important role in many successful hypersonic vehicles owing to its high aerodynamic efficiency and high plot rate. Therefore, researches on the transition problem of lifting body aircraft can help better understand the transition phenomena and related mechanisms of real aircraft, improve the capability of transition prediction, and serve the design of this type of aircraft. Therefore, the standard model design in this paper takes the lifting body as the background aircraft.

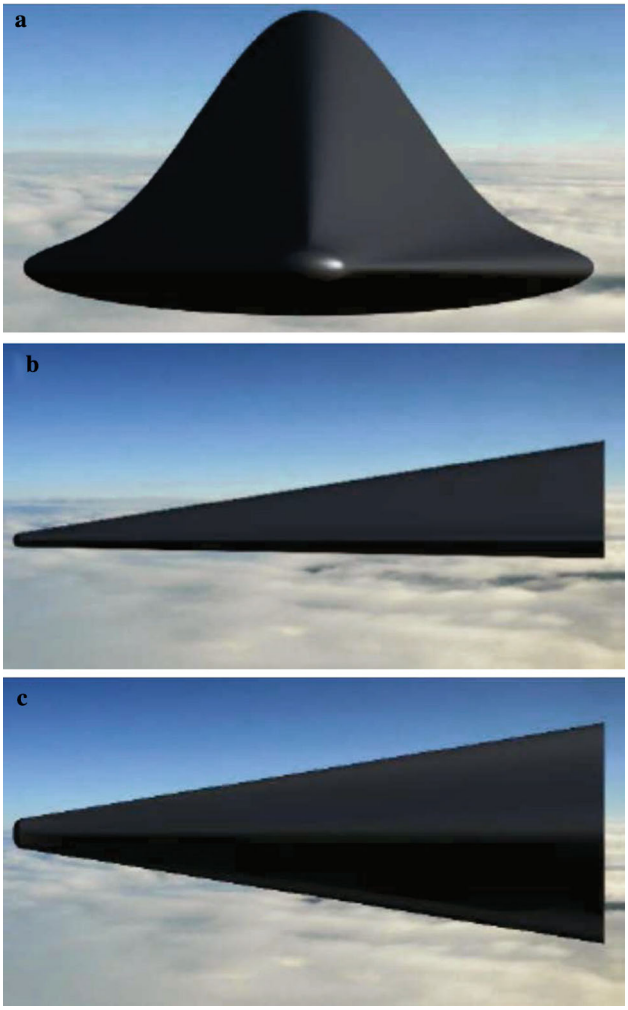

Fig. 1 Three perspective views of the standard model. **a** Front view. **b** Side view. **c** Top view

In order to pursue a higher aerodynamic efficiency, hypersonic flight vehicles generally have a highly swept delta wing and a flat lower surface. Considering the thermal protection problem at high Mach numbers, the head and leading edge are usually blunted. The windward surface mainly provides the lift, while the leeward side provides the loading space through a closed curve. Therefore, the configuration proposed in this study has the typical features of an elliptical ball head and a highly swept delta wing, as shown in Fig. 1. Meanwhile, a special design was made for the cross-section profile to meet the research requirements of the streamwise vortex induced transition, the cross-flow transition, and the attachment-line transition, with the consideration of the aerodynamic efficiency. The windward surface is designed as a relatively flat elliptical curve (the ratio of the long to the short axis is 4:1), and the leeward surface is designed as a brimmed hat shape using the class function and shape function transformation technique (CST) [30–32]. Such a shape design can meet the

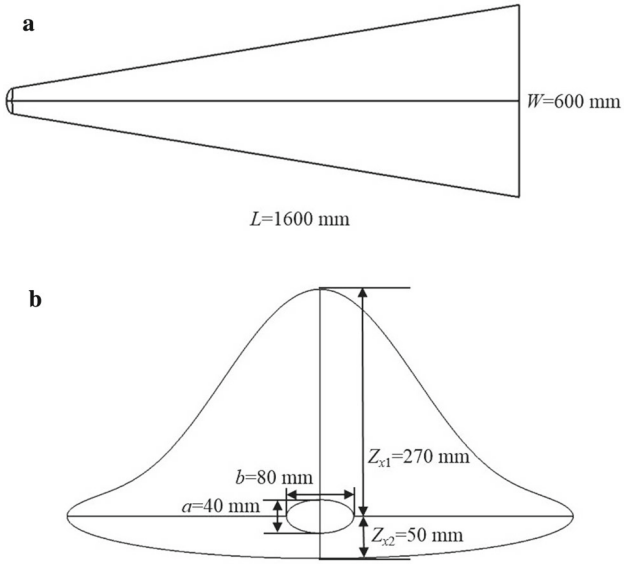

Fig. 2 Geometric size of the standard model. **a** Top view. **b** Front view

requirements of both the analytical expression and the loading space during the flight test. In addition, a waist-like shape is formed due to the shrinkage on both sides of the leeward surface, which is not only conducive to generating a vortex lift, but also conducive to enhancing the lateral and heading stability, which is good for the flight control. Figure 2 shows the geometric size of the configuration.

2.2 Parameterization method of standard model

In order to ensure that the standard model configuration can be described analytically, the parameterization of this standard model has been performed. The specific analytical design method of the standard model is explained in the following sections.

2.2.1 Parameterization of head configuration

Given the length L and width W of the standard model, the minor axis length a (the length of the central axis is equal to the length of the minor axis) and the major axis length b of the head ellipsoid, we can determine the expression of the head of the ellipsoid, i.e.,

$$\frac{(x-\frac{a}{2})^2}{(\frac{a}{2})^2}+\frac{y^2}{(\frac{b}{2})^2}+\frac{z^2}{(\frac{a}{2})^2}=1,\quad x\in[0,\frac{a}{2}]. \tag{1}$$

For each given section with the location $x_H = x_h$, $x_h \in [0, \frac{a}{2}]$, an elliptic curve described by the following formula can be obtained, i.e.,

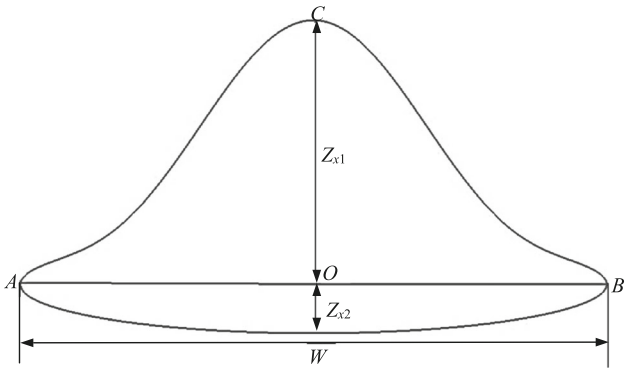

Fig. 3 Schematic of the bottom cross section with parameters indicated

$$\begin{cases} y_H = \sqrt{1 - \frac{(x_h - \frac{a}{2})^2}{(\frac{a}{2})^2}}\,\frac{b}{2}\cos\theta, \\ z_H = \sqrt{1 - \frac{(x_h - \frac{a}{2})^2}{(\frac{a}{2})^2}}\,\frac{a}{2}\sin\theta, \end{cases} \tag{2}$$

with $\theta \in [0, 2\pi]$. For the semi-ellipsoid of the head, different values of θ correspond to different points on the elliptic curve at a given section. Considering that the ellipsoid head and the fuselage need to meet a smooth transition, the head used is not a complete half ellipsoid. The dividing line between the head of the ellipsoid and the fuselage is a spatial curve, rather than a line within a certain two-dimensional plane. The specific shape and dividing line of the ellipsoid are determined in conjunction with the subsequent steps discussed in the following sections.

2.2.2 Parameterization of bottom cross section

Given the width of the standard model W, the height of the upper half of the bottom section Z_{x1}, and the height of the lower half of the bottom section Z_{x2}, we can finish the bottom section shape design as shown in Fig. 3.

The lower part of the bottom section is an ellipse, and its expression is

$$\frac{y^2}{\left(\frac{W}{2}\right)^2} + \frac{z^2}{Z_{x2}^2} = 1. \tag{3}$$

Curve AB can be obtained by

$$\begin{cases} x_{AB} = L, \\ y_{AB} = \frac{W}{2}\cos\theta, \\ z_{AB} = Z_{x2}\sin\theta, \end{cases} \tag{4}$$

with $\theta \in [\pi, 2\pi]$. The upper part of the bottom section curve ACB is a linear combination of an elliptic curve and a CST curve. The expression of the CST curve is given as

$$\begin{cases} \zeta = 2^{2n}\eta^n(1-\eta)^n, \\ \eta = 0.5\cos\theta + 0.5, \theta \in [0, \pi], \\ x_{ACB1} = L,\ \ y_{ACB1} = (\eta - 0.5)W,\ \ z_{ACB1} = \zeta Z_{x1}, \end{cases} \tag{5}$$

where n is a positive integer within (1, 10]. The local features of the curve corresponding to different n are slightly different, and n is taken as 4 for the standard model in the present study. The elliptic curve superimposed by the CST curve is expressed as below:

$$\frac{y^2}{(\frac{W}{2})^2} + \frac{z^2}{Z_{x1}^2} = 1. \tag{6}$$

According to Eq. (6), the coordinate of each specific point on the elliptic curve can be obtained as

$$\begin{cases} x_{ACB2} = L, \\ y_{ACB2} = \frac{W}{2}\cos\theta, \\ z_{ACB2} = Z_{x1}\sin\theta, \end{cases} \tag{7}$$

with $\theta \in [0, \pi]$. Finally, according to the linear combination of Eq. (5) and Eq. (7), the expression of the upper part of curve ACB can be obtained, and the ratio between the two functions can be adjusted by a parameter α, i.e.,

$$z = \alpha z_{ACB1} + (1-\alpha) z_{ACB2}. \tag{8}$$

For the upper curve of the vehicle, for $n \geq 1$, the CST function tends to vanish near the endpoint. Therefore, the shape of the upper surface near the side front edge is mainly determined by the elliptic function in Eq. (7). Taking $\alpha = 1 - Z_{x2}/Z_{x1}$, the shape can have local symmetry near the vertex of the side leading edge. Therefore, the shape of the bottom cross section can also be regarded as a complete ellipse superimposed on a CST curve, thus the coordinates of the upper surface curve can be obtained as follows:

$$\begin{cases} x_{ACB} = L, \\ y_{ACB} = \frac{W}{2}\cos\theta, \\ z_{ACB} = \alpha z_{ACB1} + (1-\alpha) z_{ACB2}, \end{cases} \tag{9}$$

with $\theta \in [0, \pi]$. Given the coordinates of points on the upper curve, the central angle of each point can be calculated as follows,

$$\begin{cases} \rho_{ACB} = \sqrt{{y_{ACB}}^2 + {z_{ACB}}^2}, \\ \Phi_{ACB} = \arccos(\frac{y_{ACB}}{\rho_{ACB}}). \end{cases} \tag{10}$$

Figure 4 shows the composition of the head ellipsoid section and the bottom cross section. Among them, curve 1 is the cross-sectional shape of the head ellipsoid; curve 2 and

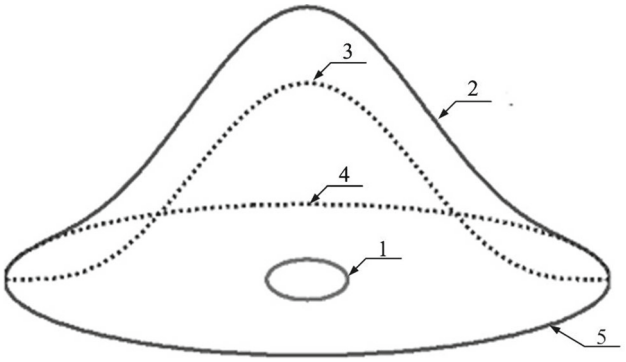

Fig. 4 Composition of the head and bottom cross section of the lifting body

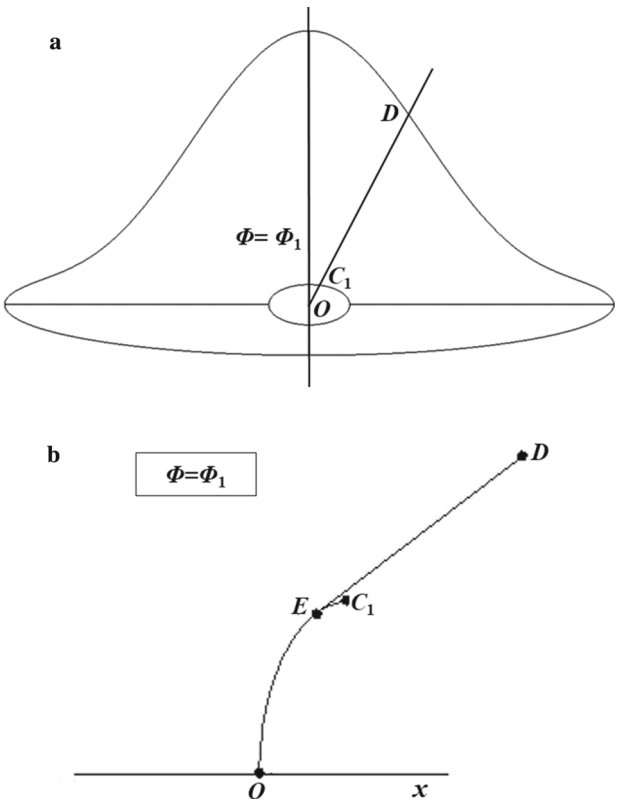

Fig. 5 Diagram of the body curve. **a** Overall view. **b** Detailed view

curve 5 are the upper and lower outlines of the bottom cross section, respectively; and the dashed lines 3 and 4 are the superimposed part of the CST curve and the elliptic curve in Eq. (8), which are superimposed together to form curve 2.

2.2.3 Parameterization of vehicle body

The method for generating the vehicle body is shown in Fig. 5. The plane with the central angle $\Phi = \Phi_1$ intersects the head of the ellipsoid with an elliptical arc $\overset{\frown}{OC}_1$, and intersects the bottom section line at point D. Point E can be found on the elliptical arc $\overset{\frown}{OC}_1$, such that the straight line ED is tangent to the elliptical arc $\overset{\frown}{OC}_1$ at point E (Fig. 5), then a smooth continuous curve $\overset{\frown}{OED}$ can be obtained. The straight line ED is the section line of the vehicle body with a central angle Φ. When Φ changes from 0 to 2π, we can get the three-dimensional shape of the vehicle body. In the cylindrical coordinate system, the coordinates of point E can be obtained by the expression of the elliptical arc $\overset{\frown}{OC}_1$ and the coordinates of point D, i.e.,

$$\begin{cases} x_E = \frac{a}{2} - \frac{a}{2}\sin\gamma, \\ \rho_E = \beta\cos\gamma, \end{cases} \tag{11}$$

where ρ_E is the distance from point E to the x-axis, and γ satisfies

$$\begin{cases} x_0 = L - \frac{a}{2}, \\ \beta = [\frac{\cos^2\Phi}{(\frac{a}{2})^2} + \frac{\sin^2\Phi}{(\frac{b}{2})^2}]^{-1/2}, \\ \cos\gamma = \frac{\beta\rho_D(\frac{a}{2})^2 + \beta x_0\sqrt{{\rho_D}^2(\frac{a}{2})^2 + \beta^2 x_0^2 - \beta^2(\frac{a}{2})^2}}{{\rho_D}^2(\frac{a}{2})^2 + \beta^2 x_0^2}, \end{cases} \tag{12}$$

where ρ_D is the distance from point D to the x-axis in Fig. 5, which can be obtained via Eq. (5) and Eq. (10); β is a function of Φ, which can be obtained by Eq. (5) and Eq. (10). Thus, the slope of the straight line ED is

$$k = \frac{\rho_D - \beta\cos\gamma}{x_0 + (\frac{a}{2})\sin\gamma}. \tag{13}$$

Therefore, the expression of the coordinate points on the lifting body at a given x location is

$$\begin{cases} \rho = \rho_E + k(x - x_E), \\ y = \rho\sin\Phi, \\ z = \rho\cos\Phi. \end{cases} \tag{14}$$

So far, the specific shape of the ellipsoid head has been determined. The interface on the ellipsoid head is irregular, which is caused by the dissimilar outlines between the bottom section and the head section. Based on Eqs. (1) and (14), the fully analytical and smooth three-dimensional shape of the lifting body can be determined. Such a lifting body model is named HyTRV in the following hypersonic boundary layer transition studies, and the transition characteristics will be discussed in details.

3 Transition characteristics of HyTRV model

Based on the above designed HyTRV model, we have performed a series of transition studies, including the linear

stability analysis, the direct numerical simulation (DNS) [33–36], and the wind tunnel experiment, and complex transition phenomena have been observed on the surface of HyTRV. The transition results from different approaches agree qualitatively well with each other, satisfying the original goal of the design of HyTRV for transition studies.

3.1 Linear stability analysis

3.1.1 Characteristics of base flow

One typical wind tunnel flow condition is chosen for the boundary layer stability study of HyTRV. The freestream flow conditions are as follows: Mach number $Ma_\infty = 6$, temperature $T_\infty = 97$ K, unit Reynolds number $Re_\infty = 1.1 \times 10^7$, and angle of attack $\alpha = 0°$. The baseflow is calculated using a high-order numerical simulation platform based on a weighted compact nonlinear scheme (WCNS), where the inviscid terms are discretized using a 5th-order explicit finite difference scheme, i.e., WCNS-E-5, while the viscous terms are solved with a 5th-order staged grid method, and the grid derivatives are specially treated with a conservation scheme. Such a platform has been validated and widely used in a range of complex flow applications [37–39]. Figure 6 shows the base flow characteristics of HyTRV. On the lower surface, the streamlines converge towards the centreline from both sides, leading to a large area of cross-flow region; while on the upper surface, the streamlines are concentrated in the concave region, resulting in two cross-flow regions on both sides. In the meantime, mushroom-like streamwise vortices are formed in the flow concentrated regions, which can be clearly seen from the streamwise velocity contour at the cross section of $x = 1450$ mm in Fig. 6b. Due to the geometry constrain, the streamwise vortex on the lower surface (LSV) is symmetric, while such a symmetry is lost for the streamwise vortex on the upper surface (USV). Furthermore, there are two attachment lines: one is located on the side of the model, which separates the flow on the lower surface from that on the upper surface; the other one is on the top of the upper surface, which separates the flow on the upper-left from that on the upper-right.

In the presence of angles of attack, the cross flow on the lower surface is attenuated, and LSV is strongly compressed which eventually disappears at $\alpha = 10°$. For USV, as the angle of attack is increased, it moves towards the top attachment line, and the flow separation occurs in the concave region. Such a change has been thoroughly investigated by Chen et al. [28].

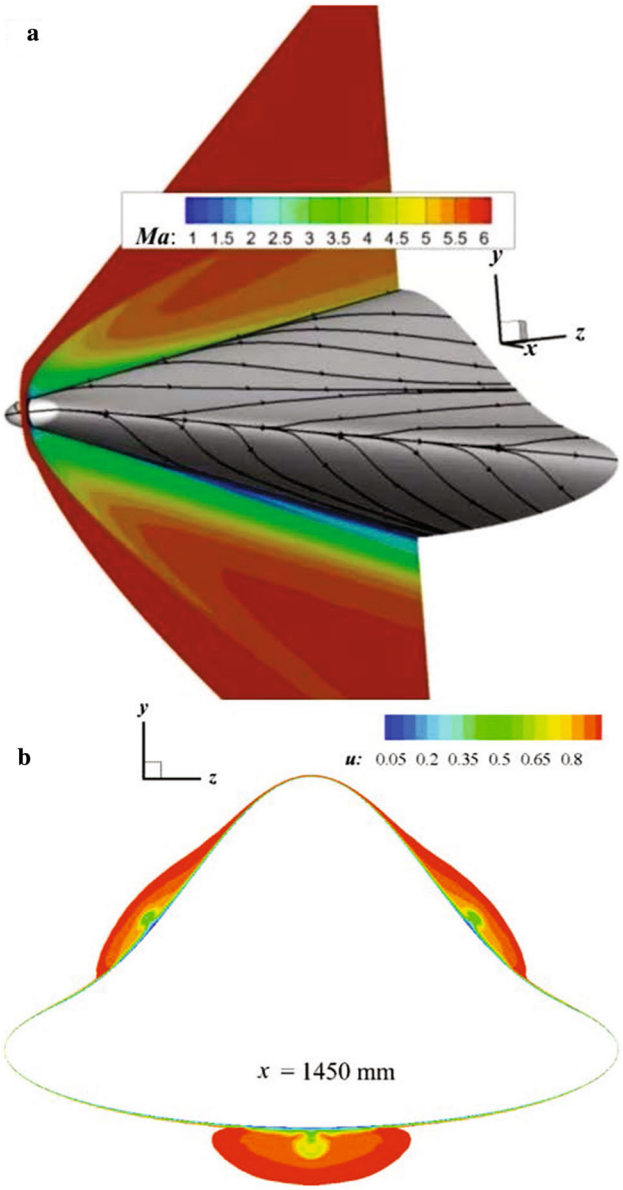

Fig. 6 Characteristics of the base flow on HyTRV: **a** Mach number contour on the symmetric plane and the surface extreme streamlines; **b** streamwise velocity contour at the cross section of $x = 1450$ mm.

3.1.2 Transition regions

LST is applied to the above obtained base flow of HyTRV at zero angle of attack to analyze its instability. LST calculates the spatial growth rate, $\alpha_i(\omega)$, of disturbances with different angular frequencies, which can be integrated along the inviscid streamlines to obtain the N-factor for each frequency, $N(\omega)$. The envelop of $N(\omega)$ at all frequencies gives the N-factor at each spatial location. Figure 7 shows the distribution of N-factors for all frequencies on the upper and lower surfaces of HyTRV, where a larger N-factor value indicates a higher likelihood of transition. Based on the N-factor distribution, it can be seen that there are six relatively independent transition regions, which from the bottom to the top are: R1-streamwise vortex region on the lower surface, R2-crossflow region on the lower surface, R3-attachment-line region on

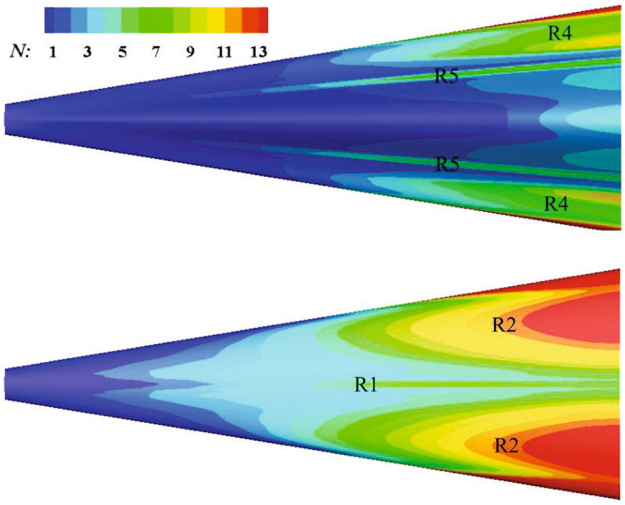

Fig. 7 N-factor contours on the upper and lower surfaces of HyTRV for all frequencies

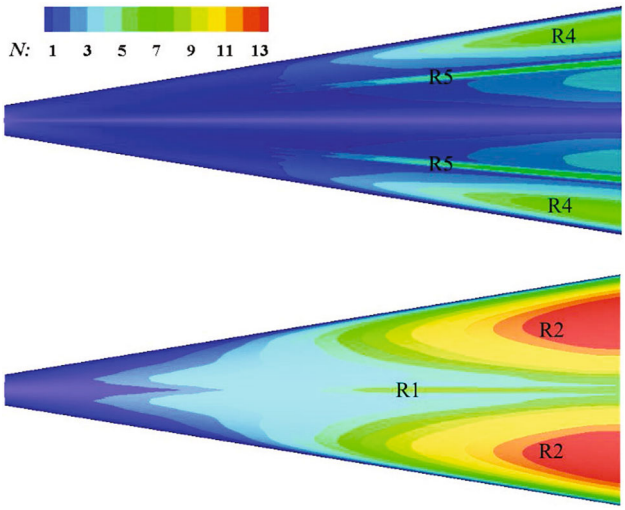

Fig. 8 N-factor contours on the upper and lower surfaces of HyTRV for the frequency range of [0, 20] kHz

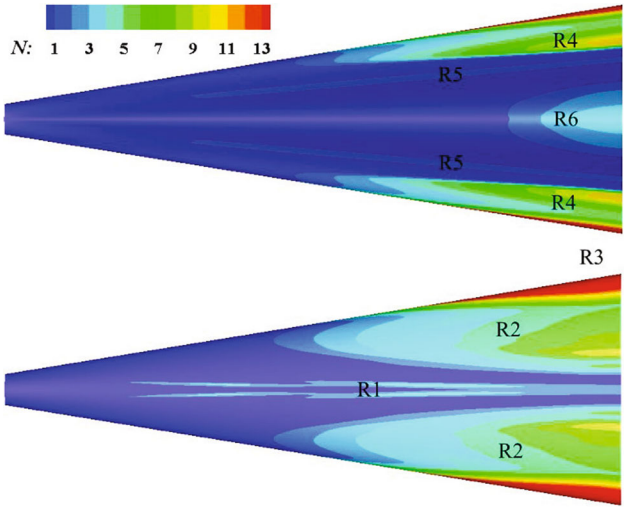

Fig. 9 N-factor contours on the upper and lower surfaces of HyTRV for the frequency range of [100, 3000] kHz.

the waist, R4-crossflow region on the waist, R5-crossflow region on the upper surface, R6-attachment-line region on the upper surface. It is worth mentioning that as the flow varies strongly in both wall-normal and azimuthal directions of R1 and R5 (see Fig. 6b), LST is not able to accurately predict the N-factor in these regions, instead, a global stability analysis approach is required [10,40], which is currently ongoing.

To clarify the dominant unstable modes in each transition region, the frequency integration range for the N-factor calculation is further divided into two sections, i.e., section I with [0, 20] kHz, corresponding to the steady and low-frequency unsteady crossflow modes, and section II with [100, 3000] kHz, corresponding to the high-frequency second mode. It is worth noting that there is no unstable mode in the frequency range [20, 100] kHz, thus the N-factor for this frequency range is not displayed. The N-factors for the two frequency ranges are shown in Figs. 8 and 9, respectively. R2 is dominated by the crossflow instability, R3 and R6 by the second mode instability, and R4 by both the crossflow mode and second mode instabilities. More LST analyses on HyTRV can be found in Ref. [28]. R1 and R5 are dominated by the instability of streamwise vortices, which will be quantified using DNS data in the following section. Overall, the rich transition phenomena on the surface of HyTRV involve four main transition mechanisms, i.e., the crossflow instability transition, the second-mode instability transition, the attachment-line instability transition, and the streamwise vortex induced transition, which satisfy the goal of HyTRV design in the transition study.

3.2 Direct numerical simulation study

To further understand the transition mechanism, very large scale direct numerical simulations have been performed for HyTRV using the open source code OpenCFD [41]. The setup of simulation requires two procedures: (1) a laminar baseflow for the half model of HyTRV including the nose-tip obtained by using a spatial second-order finite volume (FV) method, with the time advancement using the LU-SGS scheme; (2) a thin sub-domain containing the boundary layer but with the nose-tip cut off at $x = 50$ mm is used for the high-order finite difference (FD) calculation, where the convection terms are discretized with a 7th-order WENO scheme, viscous terms with a 6th-order center difference scheme, and the time marching with a 3rd-order Runge-Kutta scheme. The boundary conditions for the FD calculation are interpolated from the laminar baseflow of the FV calculation. The

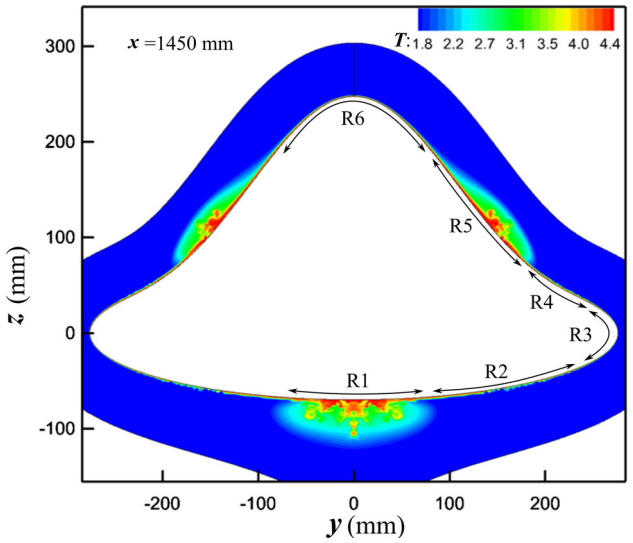

Fig. 10 Temperature contour at the cross section of $x = 1450$ mm.

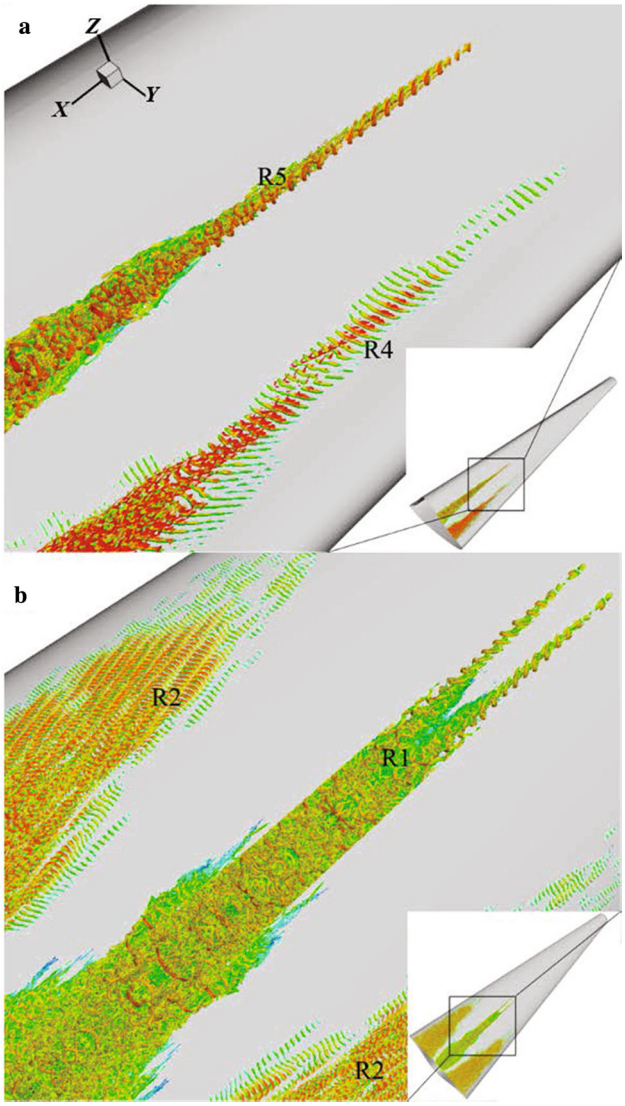

Fig. 11 Quasi-streamwise vortices visualized by Q criteria ($Q = 0.001$) and colored by the streamwise velocity for HyTRV on **a** the upper surface, and **b** the lower surface. The zoomed-in region is indicated by a black square in the inserted plot of each figure

number of grid points along the streamwise, wall-normal, and azimuthal directions is 3000, 161, and 3200 respectively, and the total grid number reaches 1.5 billion. The wall-normal grid resolution is $\Delta y^+_{\text{min}} \simeq 0.45$ for the first layer of grid (the superscript $+$ indicates scaled by viscous units), and the streamwise and spanwise grid resolutions satisfy $\Delta x^+ < 10$ and $\Delta z^+ < 10$, over majority of the HyTRV surface. To trigger the boundary layer transition, a random blowing and suction region is put in the upstream within the region $x \in [50, 60]$ mm. The flow condition is the same as the one used for the LST analysis in the previous section, except that the freestream temperature is slightly lower, i.e., $T_\infty = 79$ K. Figure 10 shows the temperature contour at the cross section of $x = 1450$ mm along the streamwise direction. Compared to Fig. 6, both LSV and USV break down, and the crossflow regions on both the lower and upper surfaces appear to be chaotic. By taking a close look at the flow details, it can be concluded that boundary layer transition occurs in four different regions, i.e., R1, R2, R4, and R5, which confirms the linear stability analysis results [28]. The number of streamwise grid points has also been doubled to 6000 to check the grid resolution effect, which gives a total grid number of 3 billion. Although the transition fronts slightly move downstream, the four transition regions remain the same.

To further visualize the flow features in different transition regions of HyTRV, Fig. 11 shows the quasi-streamwise vortices in R1, R2, R4, and R5. Although transition appears in all the four regions, the vortex structures are very different in the early state of transition. In the upstream of R1, there are two groups of hairpin vortex trains, which are distributed symmetrically about the central plane. As these hairpin vortices evolve downstream, they break down into finer structures and spread in the spanwise direction. Similar to R1, the vortex structures in R5 show the same behavior of vortex breakdown leading to transition. However, due to the lack of geometric symmetry in R5, there is only a single group of hairpin vortex train. For R2 and R4, the second mode and the crossflow mode co-exist in the flow. The second mode is featured with spanwise rollers in the upstream, which break down due to the secondary instability as they evolve downstream. In the meantime, due to the crossflow effect (Fig. 6a), there appears to be steady and unsteady crossflow vortices, aligning at a certain angle with respect to the streamwise direction, which is more obvious in R2 compared to R4. Again, these crossflow vortices break down into finer vortex structures (bamboo-shaped vortices) in the downstream due

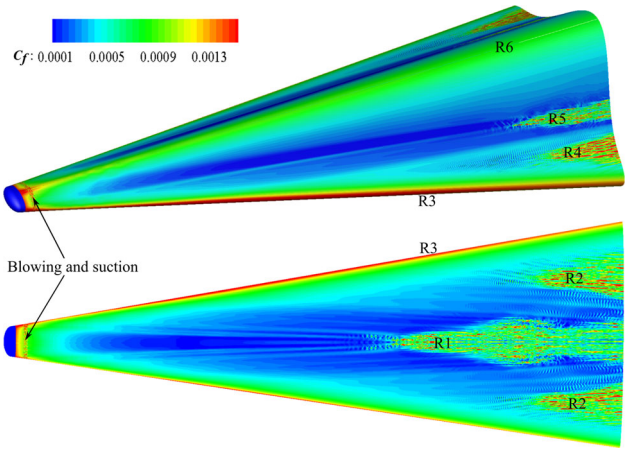

Fig. 12 Skin friction coefficient distribution on the upper and lower surfaces of HyTRV

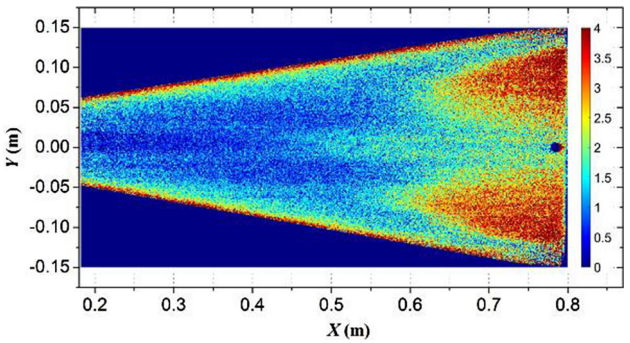

Fig. 13 Heat flux distribution measured by TSP on the lower surface of HyTRV

to secondary instabilities. Based on the features of vortex structures, it can be concluded that R2 is dominated by the crossflow instability, and R4 is dominated by both the second mode and the crossflow mode instabilities, in agreement with the findings from the previous linear stability analysis.

The vortex structures lift low-speed fluid in the near-wall region into the outer region via the so-called ejection event, while in the meantime they bring high-speed fluid from the outer region into the near-wall region via the so-called sweep event, which leaves footprints on the wall and results in a significant increase of skin friction and heat flux [42]. Figure 12 shows the skin friction coefficient, C_f distribution on the upper and lower surfaces of HyTRV, where high wall shear can be clearly seen in each transition region. The skin friction distribution is in good agreement with that of the vortex structures in R1, R2, R4, and R5. Due to the existence of the attachment-lines, high wall shear also appears in R3 and R6, but there is no rise of skin friction along the streamwise direction, indicating that transition does not occur in R3 and R6.

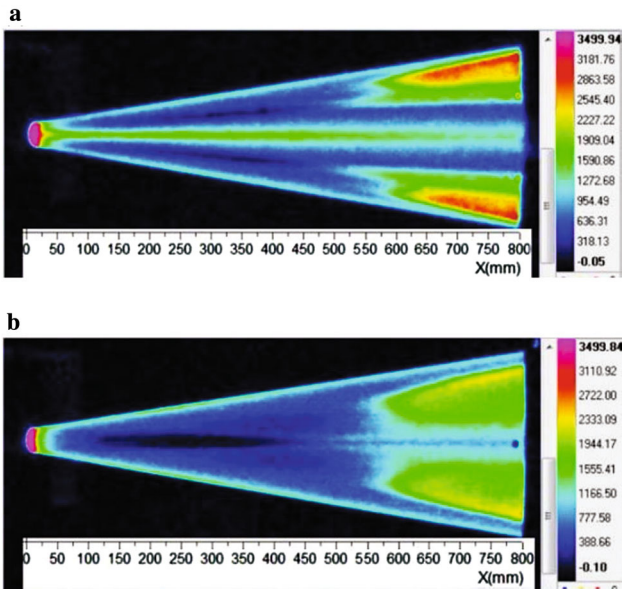

Fig. 14 Temperature distribution measured by the infrared calorimetry on the upper and lower surfaces of HyTRV. **a** Upper surface. **b** Lower surface

3.3 Wind tunnel experiment investigation

A 1:2 scaled-down model of HyTRV is used for the experimental study of boundary layer transition in two wind tunnels at CARDC, i.e., the Φ2m shock wave wind tunnel and the Φ1 m hypersonic wind tunnel. Here, only experimental results under the same flow conditions as the previous linear stability analysis are selected for presentation. Figure 13 shows the heat flux distribution on the lower surface of HyTRV measured by the temperature sensitive paste (TSP) in the Φ2 m shock wave wind tunnel, which captures the transition pattern of R2, with typical features of "double-lung lobes" similar to that observed for HIFiRE-5 [43]. It is noted that there is a slight asymmetry between the left and right lobes, which might be due to the possible non-uniformity in the freestream noise of the wind tunnel and the surface roughness of the manufactured HyTRV model.

Figure 14 shows the temperature distribution on both the upper and lower surfaces of HyTRV measured by the infrared calorimetry in the Φ1 m hypersonic wind tunnel under a similar flow condition. The transition pattern on the lower surface again shows the "double-lung lobes" feature representing the crossflow transition in R2. The temperature distribution on the upper surface shows the transition patterns of R4 and R5. High heat flux also appears in R3 and R6, but there is no such a jump along each attachment-line, indicating that no transition occurs as observed from the skin friction distribution in the DNS (Fig. 12). As the DNS missed the real receptivity process of HyTRV to the freestream disturbances, this results in different transition fronts, especially for the R1 and

R5, where strong streamwise vortices exist. However, distinguished transition patterns qualitatively agree with each other between the experimental and DNS results.

4 Conclusions

In this work, we have designed a standard model named HyTRV for the study of hypersonic boundary layer transition. We first gave the details of the configuration design and the parametric study of model; then various approaches including linear stability analyses, direct numerical simulations, and wind tunnel experiments, were combined to understand the laminar-turbulent transition characteristics of this model, which leads to the following conclusions.

(1) HyTRV model is designed using the concept of feature extraction and simplification, thus can represent the characteristics of current hypersonic lifting-body vehicles, and meet the requirement of a simple aerodynamics configuration from both numerical simulations and wind tunnel experiments. Moreover, the configuration of HyTRV has an analytical expression, which is helpful for academia communication as it can eliminate the error caused in building the numerical model.
(2) Baseflow characteristics of HyTRV suggests that cross-flow regions exist on both the lower and upper surfaces. In the meantime, streamwise vortices are formed along the centerline of the lower surface, as well as the concave region of the upper surface. HyTRV has complex transition phenomena in relatively independent areas, which is good for the transition study.
(3) Linear stability analyses, direct numerical simulations, and wind tunnel experiments all confirm that there are six relatively independent transition regions on HyTRV, including the streamwise vortex instability, the cross-flow instability, the second mode instability, and the attachment-line instability, which can satisfy the study of different transition mechanisms. However, a quantitative comparison of the transition fronts among the three methods is still challenging due to the difficulty in quantifying the receptivity process.

Based on the present study, the designed HyTRV model has typical features of lifting-body flight vehicles and also an analytically expressed configuration, which can represent multiple transition mechanisms, such that HyTRV can well support the study of fundamental problems in the laminar-turbulent transition for complex configurations.

Acknowledgements This work was supported by the National Natural Science Foundation of China (Grant 11702315, 92052301) and the National Key Research and Development Program of China (Grant 2016YFA0401200).

References

1. Chen, J.Q., Zhang, Y.F., Xu, G.L., et al.: Hypersonic boundary layer transition: what we know, where shall we go. Acta Aerodyn. Sin. **353**, 311337 (2017). (**in Chinese**)
2. Zhou, H., Su, C.H., Zhang, Y.M.: Transition Mechanism and Prediction of Hypersonic Boundary Layer. Science Press, Beijing (2015). (**in Chinese**)
3. Chen, J.Q., Yuan, X.X., Tu, G.H., et al.: Recent progresses on hypersonic boundary-layer transition. Sci. Sin.-Phys. Mech. Astron. **49**, 114701 (2019). https://doi.org/10.1360/SSPMA-2019-0071. (**in Chinese**)
4. Li, F., Xie, S.F., Bi, Z., et al.: Experimental study of several aerodynamic problems on hypersonic vehicles. Mod. Defence Technol. **42**(5), 1–7 (2014). (**in Chinese**)
5. Zhou, L., Yan, C., Hao, Z.H., et al.: Transition model and transition criteria for hypersonic boundary layer flow. Acta Aerodyn. Sin. **37**(4), 1092–1102 (2016). (**in Chinese**)
6. Luo, J.S.: Transition and prediction for hypersonic boundary layers. Acta Aeronaut. Sin. **36**(1), 357–372 (2015)
7. Schneider, S.P.: Development of hypersonic quiet tunnels. J. Spacecraft Rockets. **45**(4), 641–664 (2008)
8. Mack, L.M.: Boundary-layer linear stability theory. Rept. 709, Agard, pp. 1–18 (1984)
9. Herbert, T.: Parabolized stability equations. Annu. Rev. Fluid. Mech. **29**, 245–283 (1997)
10. Theofilis, V.: Global linear instability. Annu. Rev. Fluid. Mech. **43**, 319–352 (2011)
11. Herbert, T.: Secondary instability of boundary layers. Annu. Rev. Fluid. Mech. **20**, 487–526 (1988)
12. Wu, X.: Nonlinear theories for shear flow instabilities: physical insights and practical implications. Annu. Rev. Fluid. Mech. **51**, 451–485 (2019)
13. Zhong, X., Wang, X.: Direct numerical simulation on the receptivity, instability, and transition of hypersonic boundary layers. Annu. Rev. Fluid. Mech. **44**, 527–561 (2012)
14. Cebeci, T., Shao, J.P., Chen, H.H., et al.: The preferred approach for calculating transition by stability theory. In: Proceeding of International Conference on Boundary and Interior Layers, Toulouse, Onera (2004)
15. Wang, L., Fu, S.: Modelling flow transition in a hypersonic boundary layer with Reynolds-Averaged Navier–Stokes approach. Sci. China Phys. Mech. Astron. **52**(5), 768–774 (2009)
16. Menter, F.R., Langtry, R.B., Likki, S.R., et al.: A Correlation-based transition model using local variables: Part I model formulation. Asme Turbo Expo. GT2004-53452 (2004)
17. Fu, S., Wang, L.: Progress in turbulence/transition modelling. Adv. Mech. **37**(3), 409–416 (2007). (**in Chinese**)
18. Xiang, X.H., Zhang, Y.F., Chen, J.Q., et al.: Progress in transition models for cross-flow instabilities. Acta Aerodyn. Sin. **36**(2), 254–264 (2018). (**in Chinese**)
19. Kimmel, R.L.: Aerothermal design for the HIFiRE-1 flight vehicle. AIAA-2008-4034. Reston: AIAA-2008
20. Barrio, A.M., Sudars, M., Aulisio, R., et al.: EXPERT-the ESA experimental re-entry test-bed trajectory and mission design. AIAA 2011–6342 (2011)
21. Chen, F.J., Berry, S.A.: HyBolt flight experiment, NASA/TM-2010-216725. NASA, Washington, DC (2010)
22. Bradley, M.W., Dennis, C.B., Thomas, D.W., et al.: Boundary layer transition (BOLT) flight experiment overview. AIAA-2018-2892. AIAA Aviation Forum. Atlanta, Georgia (2018)

23. Tu, G.H., Wan, B.B., Chen, J.Q., et al.: Investigation on correlation between wind tunnel and flight for boundary layer stability and transition of MF-1 blunt cone. Sci. Sin.-Phys. Mech. Astron. **49**, 124701 (2019). https://doi.org/10.1360/SSPMA-2019-0162. (**in Chinese**)
24. Tu, G.H., Wan, B.B., Chen, J.Q., et al.: Investigation on correlation between wind tunnel and flight for boundary layer stability and transition of MF-1 blunt cone. Sci. China Phys. Mech. Astronom. **49**, 124701 (2019). (**in Chinese**)
25. Paredes, P., Gosse, R., Theofilis, V., et al.: Linear modal instabilities of hypersonic flow over an elliptic cone. J. Fluid Mech. **804**, 442–466 (2016)
26. Thome, J., Knutson, A., Candler, G.V.: Boundary layer instabilities on BolT subscale geometry. AIAA 2019–0092 (2019)
27. Chen, X., Chen, J.Q., Dong, S.W., et al.: Stability analyses of leeward streamwise vortices for a hypersonic yawed cone at 6 degree angle of attack. Acta Aerodyn. Sin. **38**(2), 299–307 (2020)
28. Li, X., Chen, J., Huang, Z., et al.: Stability analysis and transition prediction of streamwise vortices over a yawed cone at Mach 6. Phys. Fluids. **32**, 124110 (2020)
29. Chen, J., Tu, G., Wan, B., et al.: Characteristics of flow field and boundary-layer stability of hypersonic transition research vehicle (HyTRV). Acta Aeronaut. Astronaut. Sin. **42**(4), 124317 (2021)
30. Tang, W., Feng, Y., Yang, X.F., et al.: Practices of aerodynamic configuration design for non-ballistic trajectory vehicles. Phys. Gases **2**(1), 1–12 (2017). (**in Chinese**)
31. Feng, Y., Tang, W., Ren, J., et al.: Parametric geometry representation method for hypersonic vehicle configuration. Acta Aerodyn. Sin. **30**(4), 546–550 (2012)
32. Brenda, M.K.: A universal parametric geometry representation method-"CST". AIAA 2007-62 (2007)
33. Feng, Y., Tang, W., Xiao, G., et al.: Aerodynamics configuration conceptual design for X-37 analog transporter. Acta Aerodyn. Sin. **31**(1), 94–98 (2012)
34. Lin, L.M., Tan, Z.R.: DNS in evolution of vorticity and sign relationship in wake transition of a circular cylinder: (pure)mode A. Acta Mech. Sin. **35**, 1131–1149 (2019)
35. Qian, J.X., Huang, W.X., Xu, C.X.: Direct numerical simulation of turbulent boundary layer over an anisotropic compliant wall. Acta Mech. Sin. **35**, 384–400 (2019)
36. Yang, S., Xu, C.X., Wang, L.L.: Transient growth in turbulent particle-laden channel flow. Acta Mech. Sin. **36**, 1–11 (2020)
37. Zou, H.Y., Zhou, W.F., Chen, X., et al.: Boundary layer structure in turbulent Rayleigh-Bénard convection in a slim box. Acta Mech. Sin. **35**, 713–728 (2019)
38. Tu, G.H., Deng, X.B., Mao, M.L.: A staggered non-oscillatory finite difference method for high-order discretization of viscous terms. Acta Aerodyn. Sin. **29**(1), 10–15 (2011). (**in Chinese**)
39. Deng, X., Mao, M., Tu, G., et al.: Geometric conservation law and applications to high-Order finite difference schemes with stationary grids. J. Comput. Phys. **230**(4), 1100–1115 (2011)
40. Deng, X.G., Zhang, H.X.: Developing high-order weighted compact nonlinear schemes. J. Comput. Phys. **165**, 24–44 (2000)
41. Li, X.L., Fu, D.X., Ma, Y.W.: Direct numerical simulation of hypersonic boundary layer transition over a blunt cone with a small angle of attack. Phys. Fluids **22**, 025105 (2010)
42. Jeong, J., Hussain, F., Schoppa, W., et al.: Coherent structures near the wall in a turbulent channel flow. J. Fluid Mech. **332**, 185–214 (1997)
43. Juliano, T.J., Borg, M.P., Schneider, S.P.: Quiet tunnel measurements of HIFiRE-5 boundary-layer transition. AIAA J. **53**(4), 832–846 (2015)